

Role of volatiles in highly explosive basaltic eruptions

Giuseppe La Spina^{1,2✉}, Fabio Arzilli^{2,3}, Mike R. Burton², Margherita Polacci² & Amanda B. Clarke^{4,5}

Water and carbon dioxide are the most abundant volatile components in terrestrial magmas. As they exsolve into magmatic vapour, they promote magma buoyancy, accelerating ascent and modulating eruptive dynamics. It is commonly thought that an increase in pre-eruptive volatile content produces an increase in eruption intensity. Using a conduit model for basaltic eruptions, covering the upper 6 km of conduit, we show that for the same chamber conditions mass eruption rate is not affected by CO₂ content, whereas an increase in H₂O up to 10 wt.% produces an increase in eruption rate of an order of magnitude. It is only when CO₂ is injected in the magma reservoir from an external source that the resulting pressurisation will generate a strong increase in eruption rate. Results also show that ascent velocity and fragmentation depth are strongly affected by pre-eruptive volatile contents demonstrating a link between volatile content and eruptive style.

¹Istituto Nazionale di Geofisica e Vulcanologia, Osservatorio Etneo, Sezione di Catania, Catania, Italy. ²Department of Earth and Environmental Sciences, The University of Manchester, Manchester, UK. ³School of Science and Technology, Geology Division, University of Camerino, Camerino, Italy. ⁴School of Earth and Space Exploration, Arizona State University, Tempe, AZ, USA. ⁵Istituto Nazionale di Geofisica e Vulcanologia, Sezione di Pisa, Pisa, Italy.
✉email: giuseppe.laspina@ingv.it

Among the different components contained in magma, volatiles play a fundamental role in controlling magma ascent from depth^{1–10}. On Earth, the major gas species present in magmas are H₂O and CO₂, but we can also find other volatile components, such as compounds of S, Cl, and F, usually in lower concentrations^{3–19}. They are either exsolved as bubbles or dissolved in the magma, and the amount of volatiles that can stay dissolved within the melt scales with pressure¹. Exsolved volatiles increase magma buoyancy, resulting in acceleration as magma approaches the surface^{1,20}. Therefore, exsolved volatiles provide a strong driving force for magma ascent^{3,6,8,12,16,21,22}. Volatiles (exsolved and dissolved) also influence several processes during magma ascent, such as crystallisation^{4,6,15,17,23–25}, outgassing^{7,9,26–28}, temperature and rheology^{3,5,14,29,30}, significantly affecting the evolution and the style of an eruption. For example, recently Arzilli et al.³¹ showed that large undercooling (i.e. the difference between the highest temperature at which the crystals are expected to begin to crystallise and the temperature of the magma), which is strongly controlled by dissolved water content^{7,24,32}, drives exceptionally rapid crystallisation (within minutes), inducing a step change in viscosity and triggering magma fragmentation. Another example of the influence of exsolved volatiles during magma ascent is given by the effect of adiabatic cooling resulting from bubble expansion, which can alter the magmatic temperature and, thus, the ascent dynamics²⁹.

It is widely recognised that higher volatile content is usually associated with greater eruption intensity^{3,7,33}. Recently, many authors have invoked high CO₂ content to explain stronger explosive eruptions^{5,16,19,34–38}. Indeed, following Henry's law for solubility of gas mixtures in a liquid, an increase in CO₂ content has been proposed to result in more extensive exsolution of H₂O (resulting from the low solubility of the former compared with that of the latter), increasing, in turn, the buoyancy and pressure of magma, and thus the explosivity of the eruption. Although this argument is compelling, it does not consider the influence of other processes occurring during magma ascent, such as crystallisation, outgassing, thermal and rheological variations. These additional processes, due to their non-linear interdependency, can affect the eruptive activity in different ways, producing unexpected outcomes. Numerical models of magma ascent are powerful tools to investigate the role of specific volatile quantities within this strongly non-linear behaviour, and demonstrate their impact on the overall ascent dynamics in a more holistic and comprehensive approach.

Here we quantitatively investigate the influence of the two major volatiles species in magmatic mixtures, H₂O and CO₂, on the explosivity of basaltic magmas, the most common type of magma on Earth, using a multiphase, multicomponent numerical model for magma ascent, which takes into account all of the major processes occurring during magma ascent^{28,29,39–41}.

Results and discussion

Role of H₂O and CO₂ on explosive basaltic eruptions. To investigate the role of H₂O and CO₂ on highly explosive basaltic eruptions, we adopted a 1D steady-state model for magma ascent⁴¹, which has been widely used to investigate processes during magma ascent at different volcanoes^{39–45}. The governing equations adopted here are those illustrated in La Spina et al.⁴¹ and describe the ascent dynamics of a multiphase, multi-component magma in a cylindrical conduit. The application of the model to a specific volcano is achieved by providing appropriate constitutive equations, describing the specific rheological, solubility, crystallisation, outgassing, and fragmentation behaviour, together with equations of state for each component. The

complete description of the equations of the model is illustrated in the Methods section.

In this work, to investigate the role of volatiles on magma ascent dynamics we consider as a test case one of the four well-documented basaltic Plinian eruptions that have occurred on Earth: the 122 BCE Etna Plinian eruption^{31,46–50}. A total volume of 0.4 km³ dense rock equivalent was erupted, with an estimated maximum column height of 24–26 km, and an average mass eruption rate (MER) between 5 and 8.5 × 10⁷ kg s⁻¹^{46,48,50}. The mineralogical assemblage is mainly composed of plagioclase, clinopyroxene, and olivine, with phenocryst and microlite contents of 1–10 vol.% and 65–90 vol.%, respectively^{46,48,49}. Dissolved volatile content calculated from melt inclusions ranges between 1–3 wt.% water, and 200–900 ppm carbon dioxide⁴. We remark that the purpose of this work is not to simulate or reproduce exactly the Etna 122 BCE Plinian eruption. We choose this eruption as an example to investigate the role of volatiles on highly explosive basaltic eruptions.

To quantitatively study the effect of H₂O and CO₂ content on the magma ascent dynamics of basaltic explosive eruptions, we performed numerical simulations changing the initial total volatile content (exsolved + dissolved) and consequently the initial content of magma (melt + crystals), balancing the increase in gas mass by removing mass of magma, whilst fixing all the other input parameters (Fig. 1, Table 1).

Our reference simulation assumes 3.0 wt.% of H₂O and 0.9 wt.% of CO₂⁴. The simulations with higher H₂O content (named “excess H₂O simulations”) assume either 6.0 wt.% or 10 wt.% of H₂O. High CO₂ simulations (named “excess CO₂ simulations”) use either 6.0 wt.% or 10 wt.% of CO₂. These simulations with excess volatile content represent an internal redistribution of the pre-eruptive bubbles towards the top of the magma chamber due to buoyancy^{51,52} (Fig. 1). Once the saturation condition is met within the magma chamber, pre-eruptive bubbles start to nucleate and

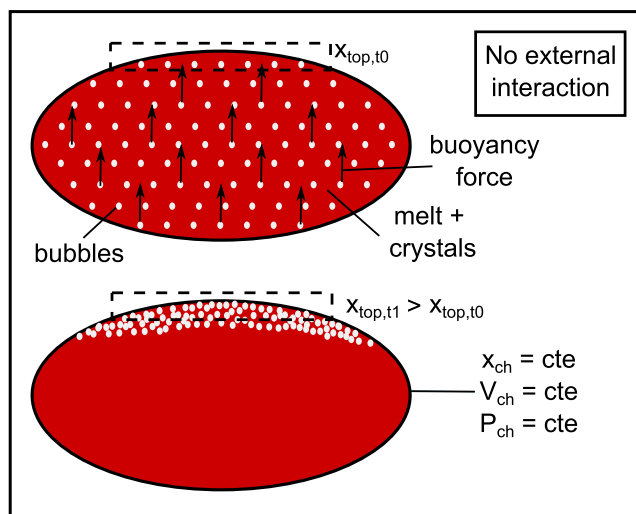


Fig. 1 Schematic representation of excess volatile accumulation at the top of the chamber due to bubble buoyancy. If the volatile saturation condition is met within the magma chamber, pre-eruptive bubbles start to nucleate and grow uniformly within the chamber (scenario at time t_0). After some time ($t_1 > t_0$), exsolved bubbles start to rise and accumulate at the top of the chamber due to buoyancy, creating an excess volatile region ($X_{top,t1} > X_{top,t0}$). Since this is simply a mechanical movement of the bubbles inside the reservoir, the overall mean parameters within the chamber remain constant (such as the total volatile content, X_{ch} , the volume of the chamber, V_{ch} , and the pressure, P_{ch}).

Table 1 Initial conditions for the reference numerical simulation of the Etna 122 BC Plinian eruption, for the excess H₂O and CO₂ runs, for the sensitivity analysis, and for external increase in H₂O and CO₂ (due to interaction with an external volatile source).

Parameter	Initial conditions for the Etna 122 BCE test case eruption					
	Reference value	Excess H ₂ O	Excess CO ₂	Sensitivity Analysis	External H ₂ O	External CO ₂
Inlet pressure [MPa]	160	160	160	140–180	191	229
Inlet temperature [°C]	1060	1060	1060	1030–1130	1060	1060
Total H ₂ O content [wt.%]	3.0	6.0; 10.0	3.0	1–10	4.0	3.0
Total CO ₂ content [wt.%]	0.9	0.9	6.0; 10.0	0.1–10	0.9	1.9
Initial crystal fraction [vol.%]	~10	~10	~10	0–20	~10	~10
Conduit radius [m]	35	35	35	10–50	35	35
Conduit length [m]	6000	6000	6000	6000	6000	6000

grow, and, if they have enough time, they ascend towards the top of the chamber due to buoyancy. This will generate a gas-rich foam at the top of the chamber (which is assumed to be the base of the conduit) without changing the overall magma chamber pressure and temperature. This implies that the inlet pressure is fixed, and further chamber overpressure due to the addition of volatiles is not considered in this first set of simulations. We remark that we used 6 and 10 wt.% of total volatiles to simulate “worst-case” scenarios, in which a very high concentration of volatiles accumulates at the very top of the magma chamber.

For all simulations, we consider a cylindrical conduit of 6 km length⁵⁰ with an inlet pressure of 160 MPa. The plagioclase phenocrysts present in the erupted products suggest an initial temperature lower than 1060–1100 °C⁵³, thus we set the inlet temperature to 1060 °C. Regarding the initial crystal content (i.e. the phenocryst content), we use a value of ~10 vol.%, in agreement with previous studies^{46,48,49}. The radius of the conduit was set to 35 m, in order to produce a MER consistent with those estimated for the Etna 122 BCE Plinian eruption. The different eruptive styles resulting from the numerical simulations are distinguished following La Spina et al.⁴¹.

As we can see from Fig. 2a, b, the pressure and the exsolved gas volume fraction along the conduit decreases as we decrease the total volatile content, and at a given depth, the greater the exsolved volatile fraction, the greater the pressure within the conduit (Supplementary Data 1). Changing the H₂O content and CO₂ content independently has different impacts on the ascent velocity (Fig. 2c). At excess H₂O content (6 and 10 wt.%) the ascent velocity at depths below ~500 m is much higher than that obtained at excess CO₂ content. However, the high ascent velocity at depth resulting from simulations with excess H₂O prevents the formation of high strain rates in the low-viscosity basaltic magma, resulting in lava fountaining eruptions rather than in powerful explosive eruptions⁴¹ (Plinian and sub-Plinian).

The different velocity profiles obtained assuming either excess H₂O or excess CO₂ are the result of both gas volume fraction and viscosity profiles along the conduit (Fig. 2b–d, Table 2). At higher total volatile content (either H₂O or CO₂), the magmatic mixture is more buoyant due to high exsolved gas volume fraction (Fig. 2b, Table 2). In general, this buoyancy should promote a faster magma ascent. However, in excess CO₂ simulations, profiles show an increased mixture viscosity of about one order of magnitude compared to the reference case (Fig. 2d, Table 2), which counterbalances the increased buoyancy of magma, resulting in similar ascent velocity with respect to the reference case (Fig. 2c, Table 2). On the contrary, in excess H₂O simulations, profiles show reduced viscosity values compared to the reference case (Fig. 2d, Table 2). The combined effects of high gas volume fractions and lower viscosities results in a large increase in magma ascent velocity for the excess H₂O simulations relative to the reference case (Fig. 2c, Table 2).

Mixture viscosity is strongly controlled by the dissolved volatile content, the temperature, and the crystal content³⁰, which, in turn, are strongly affected by the different total H₂O and CO₂ contents assumed, as shown below.

The dissolved volatile content increases as we increase the total water content (Fig. 2e), since the total dissolved volatile content is mostly water, due to the low solubility of CO₂ and the high solubility of H₂O at these depths^{21,37}. Conversely, a decrease in dissolved volatile content is obtained by increasing the CO₂ content of the system (Fig. 2e), due to the corresponding changes in partial pressures and the differences in solubility between the two volatile phases.

The temperature of the system increases as total H₂O is reduced, and decreases as total CO₂ content is reduced (Fig. 2f). These temperature trends are caused by two main competing processes: adiabatic cooling during gas expansion and release of latent heat of crystallisation²⁹. Since the system is at saturation conditions, with increasing total water, the exsolved gas volume fraction increases within the conduit (Fig. 2b), enhancing cooling due to gas expansion. On the other hand, with increasing CO₂ abundance, the dissolved volatile content decreases within the conduit (Fig. 2e) thus favouring crystallisation (Fig. 2g), and release of latent heat. The latent heat mitigates the effect of the adiabatic cooling, resulting in a relative increase in temperature compared with simulations without excess CO₂.

The variation in volatile content also affects the crystal content throughout the conduit (Fig. 2g). As we show above, both dissolved volatile content and temperature profiles are affected by the assumed total volatile contents (Fig. 2e, f). Lower dissolved volatile contents and lower temperatures promote crystallisation (due to an increase in magma undercooling)³¹. In excess CO₂ simulations, for most of the length of the conduit, we observe a decrease in dissolved volatile content (which is mostly H₂O) compared with the reference case, which promotes crystallisation. Under the same conditions, the temperature increases, which inhibits crystallisation. Numerical results show that, for these excess CO₂ simulations, the effect of the lower dissolved volatile content is stronger than the effect of higher temperature, resulting in a net increase in crystal content relative to the reference case. Following the same lines of inquiry, we find that excess H₂O simulations result in a lower crystallinity compared with the reference case. (Fig. 2e, f).

Combining the different influences that H₂O and CO₂ have on the temperature, crystal content and dissolved volatile content, our results show that an increase in CO₂ will increase the viscosity of the magma mixture throughout the conduit, whereas increasing the amount of water will decrease viscosity (Fig. 2d).

Consistent with La Spina et al.⁴¹, for the excess H₂O simulations, the eruption style shifts from lava fountaining (subaerial fragmentation) towards highly explosive eruptions (shallow fragmentation, ~140 m depth) as we decrease the total water content. When the total water content is low, the magma

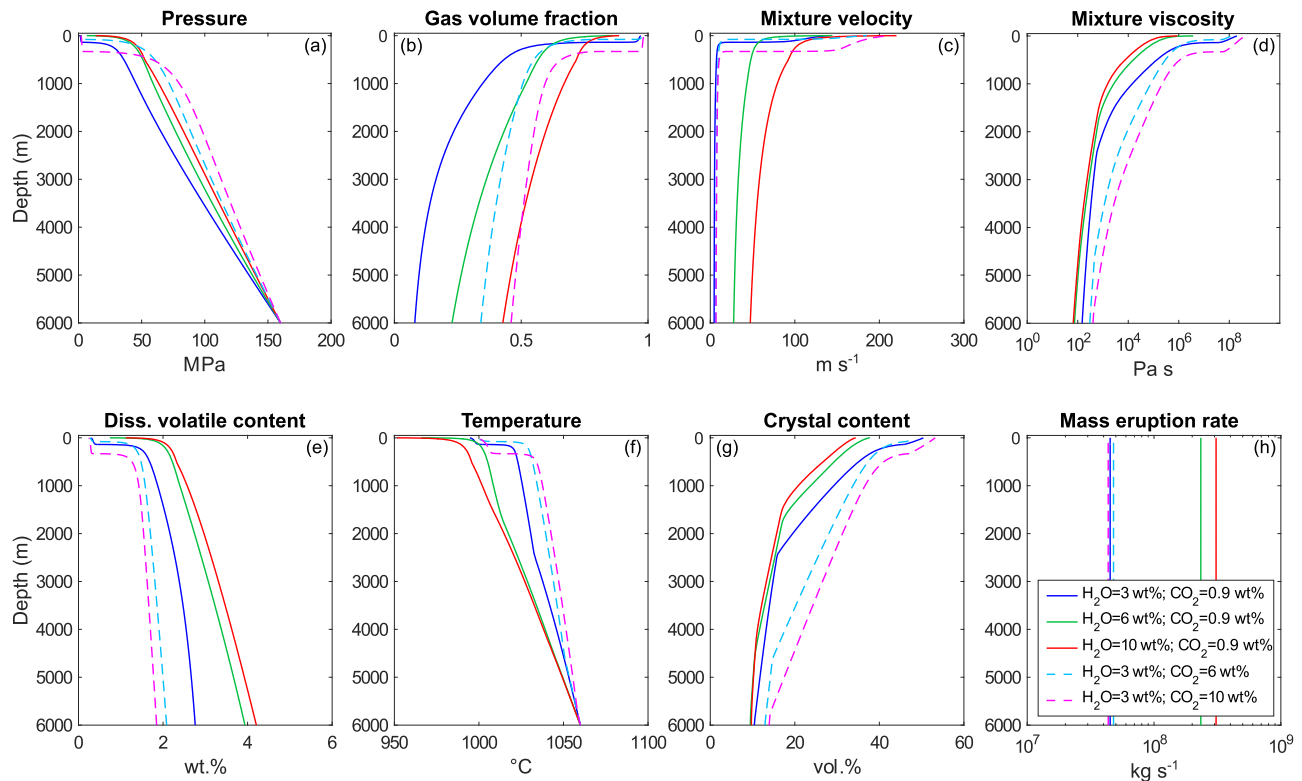


Fig. 2 Comparison of the numerical solutions for the reference and excess volatile simulations. Evolution of (a) pressure, (b) exsolved gas volume fraction, (c) mixture velocity, (d) mixture viscosity, (e) dissolved volatile content, (f) temperature, (g) total crystal content and (h) mass eruption rate (MER) along the conduit obtained for the Etna 122 BCE reference case (blue solid lines) and for the excess H₂O (green and red solid lines) and CO₂ (cyan and magenta dashed lines) case. Crystal content indicates the sum of phenocrysts and microlites content, where the phenocryst content is assumed constant throughout the conduit (equal to the initial crystal content), and only microlites are crystallising during ascent.

Table 2 Gas volume fraction, viscosity and velocity values at selected depths resulting from the reference simulation and from both the excess H₂O and CO₂ runs.

	Reference simulation	Excess H ₂ O		Excess CO ₂	
		H ₂ O = 6 wt.%	H ₂ O = 10 wt.%	CO ₂ = 6 wt.%	CO ₂ = 10 wt.%
Gas volume fraction at 3000 m	0.16	0.36	0.54	0.42	0.52
Gas volume fraction at 500 m	0.43	0.57	0.72	0.55	0.66
Viscosity at 3000 m [Pa s]	4.2×10^2	2.8×10^2	2.3×10^2	1.9×10^3	5.3×10^3
Viscosity at 500 m [Pa s]	1.3×10^5	1.6×10^4	7.4×10^3	2.9×10^5	1.1×10^6
Velocity at 3000 m [m/s]	5	33	58	7	8
Velocity at 500 m [m/s]	7	48	92	9	11

ascent velocity at depth decreases, but the exit velocity (given for most high intensity eruptions by the choked flow condition) remains similar. This results in greater magma acceleration approaching the surface, and, thus, in an increase in elongational strain rate at reduced H₂O content. Furthermore, a decrease in total H₂O content results in higher viscosity as described above. Both effects produce an increase in the Deborah number (i.e. the ratio between the Maxwell relaxation timescale and the magma deformation timescale)⁴¹ favouring magma fragmentation at lower H₂O content.

This result is counterintuitive, because, in the past, higher intensity explosive eruptions have been linked to higher water contents^{3,7,33,54}. Nevertheless, there are lines of evidence that very powerful basaltic Plinian eruptions do not require high water content^{4,55,56}, in agreement with our findings.

Contrary to the runs with excess water content, the excess CO₂ simulations show similar or slightly deeper fragmentation (~80 m

depth for CO₂ = 6wt.% and ~330 m for CO₂ = 10 wt.%) than the reference case (~140 m depth), in agreement with Papale and Polacci⁵⁴. This variation in fragmentation depth for the excess CO₂ simulations, however, does not result in strong increase in ascent velocity at depth (Fig. 2c). The increase in crystal content (Fig. 2g), and consequently in viscosity (Fig. 2d), associated with higher initial CO₂ content, results in a higher Deborah number compared with the low CO₂ simulation, facilitating deeper fragmentation.

Consistent with the magma ascent velocities at depth and exit velocities, MERs for our simulations (calculated as the mixture density multiplied by the ascent velocity and the cross-sectional area of the conduit) are essentially the same regardless of the excess volatile content. For example, for simulations ranging from 0.9 wt.% to 10 wt.% of CO₂, MERs vary only between 4×10^7 and 5×10^7 kg s⁻¹ (Fig. 1d), much less than one order of magnitude, whereas MER increases from 5×10^7 kg s⁻¹ to 3×10^8 kg s⁻¹ as

H₂O content increases from 3 wt.% to 10 wt.%, just under an order of magnitude. To the best of our knowledge, this is a very important and novel result because recently CO₂ content has been identified as a major controlling parameter on the intensity of explosive eruption^{5,16,19,34–36,38}. Our results instead indicate that CO₂ content does not detectably affect MER, whereas a large increase in H₂O may result in an increase of less than an order of magnitude in MER.

Sensitivity analysis on basaltic eruption dynamics. With the numerical simulations presented above, we investigated the role of water and carbon dioxide on the magma ascent dynamics of a highly explosive basaltic eruption compatible with the Etna 122 BCE Plinian eruption. We showed that an increase in total volatile content strongly affects magma ascent velocity within the conduit (Fig. 2c), while at the same time it has limited influence on the MER (Fig. 2h). An increase in total volatile content results in an increase in exsolved gas volume fraction (Fig. 2b), decreasing magma mixture density, which counteracts the effect of increase velocity on eruption rate. Importantly, we also found that variations in H₂O or CO₂ have a different effect on the fragmentation depth: excess H₂O changes simulated eruption styles from explosive to fire fountaining, whereas excess CO₂ leads to deeper fragmentation.

Although the numerical results presented above have been obtained for the Etna 122 BCE eruption, they can be easily generalised for any basaltic magma ascending in a cylindrical conduit from depths less than ~6 km. Accordingly, for a broader investigation of the role of H₂O and CO₂ in basaltic magma ascent dynamics, we performed a sensitivity analysis to study the influence of some input parameters (inlet pressure and temperature, radius of the conduit, total H₂O and CO₂ content, and initial crystal content) on specific output parameters (MER, melt exit velocity, and fragmentation depth). The range of input parameters adopted for the sensitivity analysis are illustrated in Table 1. The ranges for inlet pressure, inlet temperature, and total crystal content are set to account for uncertainty based on literature data for these parameters^{46,48–50,53}. For the conduit radius, we set values to produce MERs consistent with high intensity eruptions (specifically > ~10⁶ kg s⁻¹). Finally, since the focus of the manuscript is to investigate the role of volatiles for highly explosive eruptions, we set wide ranges for H₂O and CO₂ total content, to include the excess volatile scenarios investigated previously. We assumed a uniform distribution within the aforementioned ranges. The sensitivity analysis was performed on 10,000 different simulations using the DAKOTA toolkit (Design Analysis Kit for Optimisation and Terascale Applications)⁵⁷, an open-source software developed at Sandia National Laboratories that provides a flexible and extensible interface between analysis codes and iterative systems analysis methods such as uncertainty quantification, sensitivity analysis, optimisation, and parameter estimation.

As we did for the first set of simulations (Fig. 2), we highlight that for each numerical simulation the volume of molten magma (melt + crystals) is not constant, and it varies according to the initial volatile mass fraction assumed. Therefore, the overall sensitivity analysis cannot be seen as an evolution of a given magmatic system (such as describing a magma chamber that is progressively cooling or depressurising), but as a collection of different possible independent scenarios for a basaltic eruption.

Results from the sensitivity analysis (Supplementary Data 2) show that inlet temperature, which represents the pre-eruptive temperature of magma at the onset of the eruption, exerts strong control on the style of activity⁴¹, favouring powerful explosive activity at lower temperatures, and lava fountaining at higher

temperatures (Fig. 3a). The initial crystal content also has a strong influence on the eruptive style, highlighting that an increase in initial crystal content results in an increase in the occurrence of explosive eruptions (Fig. 3b). The strong control of temperature and crystal content on style of activity is related to the viscosity of the magmatic mixture, which increases with decreasing temperature and with increasing crystal content. In turn, the increase in viscosity increases the Deborah number, favouring fragmentation, which explains why we observe a larger number of highly explosive eruptions at lower temperatures and higher initial crystal content⁴¹.

The inlet pressure and the radius of the conduit exert weaker influence on the style of activity with respect to inlet temperature and initial crystal content (Fig. 3c, d). However, increased pressure and larger radii favour fountaining activities over powerful explosive eruptions. Both higher inlet pressure and larger conduit radius result in faster magma ascent at 6 km, reducing acceleration in the shallow conduit, thereby inhibiting high elongational strain rates and corresponding magma fragmentation.

Numerical results also show that water and carbon dioxide have a different influence on the style of activity at basaltic volcanoes. Higher total H₂O content results in faster magma ascent at depth (Fig. 2c), preventing acceleration and the formation of high strain rates and magma fragmentation within the conduit and therefore promoting lava fountaining over highly explosive activity (Fig. 3e). In line with the findings of La Spina et al.⁴¹, this does not preclude magma fragmentation during lava fountaining activity, but it suggests that fragmentation, if achieved, occurs above the vent. These results also confirm that it is possible to have powerful explosive eruptions even when the amount of water is relatively low (~1–3 wt.%), such as the Plinian eruptions that occurred at Masaya Volcano, Nicaragua⁵⁵, and at Tarawera, New Zealand⁵⁶ and the sub-Plinian sequence at Sunset Crater (AZ, USA)⁵⁸. In contrast, we do not observe any variation in the style of activity as a function of the total CO₂ content (Fig. 3f). Our excess CO₂ simulations show that lower CO₂ content results in shallower fragmentation depth (Fig. 2). However, results from the sensitivity analysis suggest that this is not sufficient to induce a significant change in eruption style (Fig. 3).

The different fragmentation depths obtained in the sensitivity analysis can be seen in Fig. 4a. Alongside the frequency of each output parameter, we also plotted the corresponding Sobol indices of input parameters (Fig. 4b, d, f), which are a measure of how much the variability of an output parameter is affected by the variability of a given input variable within the ranges investigated⁴⁰. As anticipated, temperature has the strongest influence on the fragmentation depth (and therefore on the style of activity), followed by the water content, carbon dioxide content and crystal content. Within the parameter space investigated here, numerical results also show that melt/particle exit velocity ranges between 40 and 300 m s⁻¹ (Fig. 4c) and that it is highly influenced by the total volatile content in the magmatic mixture (Fig. 4d). Specifically, the major controlling factor affecting exit velocity is H₂O content, followed by temperature and CO₂ content. The calculated MERs show larger values for lava fountaining activities rather than for powerful explosive eruptions (Fig. 4e), in agreement with La Spina et al.⁴¹ MER ranges from 10⁶ to 10⁹ kg s⁻¹ for highly explosive eruptions, versus 10⁷ to 10⁹ kg s⁻¹ for lava fountaining. As anticipated, the MER is not strongly affected by total volatile contents, but it is largely controlled by the radius of the conduit and inlet temperature (Fig. 4f). Therefore, our results highlight that the total volatile content has a strong influence on magma ascent velocity, but not on MER, as observed for the 2015 Calbuco eruption⁵⁰.

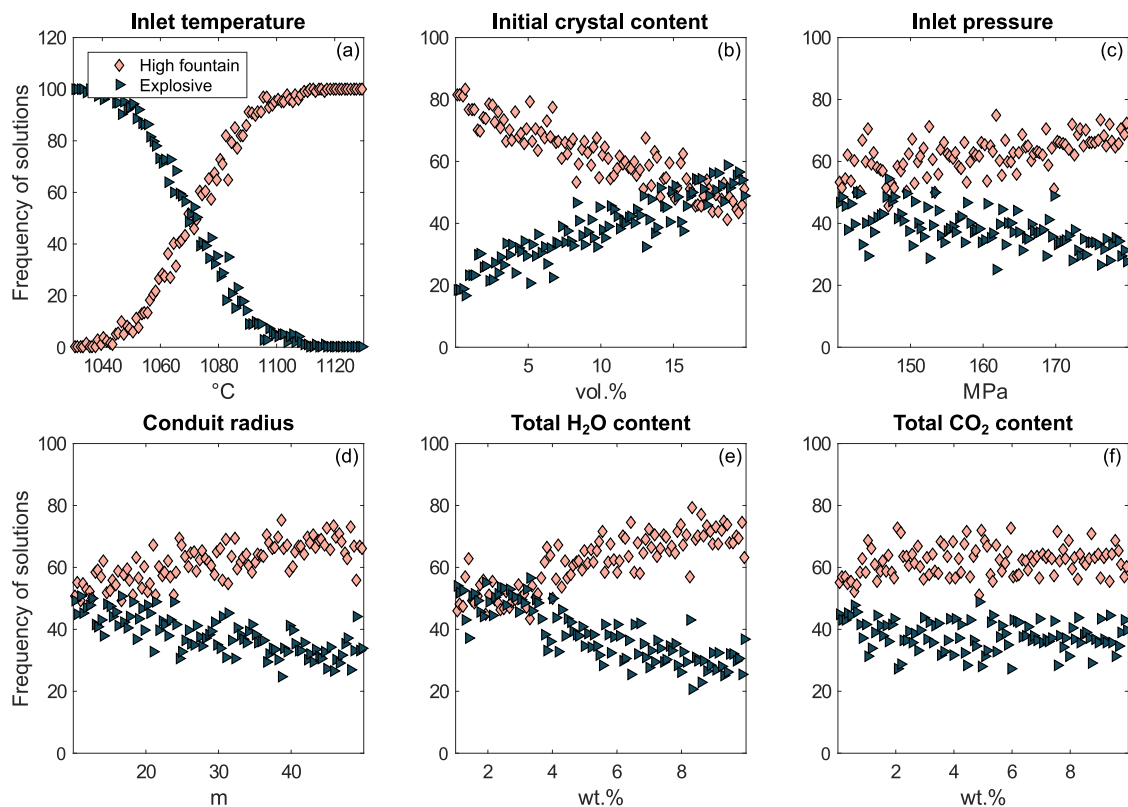


Fig. 3 Frequency of solutions as function of each input parameter resulting from the sensitivity analysis. We plot the number of solutions obtained from the sensitivity analysis as function of the input parameters: **(a)** the inlet temperature; **(b)** the initial crystal content (i.e. phenocryst content); **(c)** inlet pressure; **(d)** conduit radius; **(e)** total H₂O content; **(f)** total CO₂ content. Results are normalised as a percentage such that the sum of frequencies is always 100. Of all the 10,000 simulations performed, ~7% (mostly at low inlet temperature and low total water content) were not able to satisfy the boundary conditions at the vent of the conduit (i.e. magma is not able to reach the surface), resulting in unacceptable solutions. Since there is still a significant amount of acceptable simulations (~93%), the sensitivity analysis has not been affected by this issue. The eruptive styles are distinguished following La Spina et al.⁴¹. An “explosive” simulation (dark green triangles) is obtained when fragmentation is achieved below the vent of the conduit. If fragmentation is not met within the conduit, then ballistic jet height $H = u^2/(2g)$ is calculated. If $H > 50$ m then the simulation is marked as “high fountain” (pink diamonds); if $0.1 < H < 50$ m as “weak fountain”; if $H < 0.1$ m as “effusive”.

To analyse in greater detail the role of water and carbon dioxide contents on MER, exit velocity and fragmentation depth, we report in Fig. 5 the corresponding correlation plots derived from the sensitivity analysis.

From the numerical results we can see that a decrease in water content from 10 wt.% to 1 wt.% results in a slight decrease in MER (<1 order of magnitude, Fig. 5a). A variation in CO₂, instead, does not affect the MER at all, showing an average of $\sim 10^8$ kg s⁻¹, regardless of the amount of CO₂ considered (Fig. 5d). The exit velocity spans from ~ 50 to ~ 300 m s⁻¹ with the average ranging from ~ 140 to ~ 230 m s⁻¹ over the full range of assumed H₂O contents (Fig. 5b, cyan line), whereas average exit velocity ranges between ~ 175 and ~ 225 m s⁻¹ over the full range of CO₂ contents (Fig. 5e, cyan line). These plots show that the exit velocity decreases as the total volatile content decreases, and that it is more sensitive to a change in total water content than in total CO₂ content.

The average fragmentation depth increases with increasing water content, from 0 wt.% to roughly 3 wt.%, where basaltic magmas are saturated at a chamber depth of 6 km (140–180 MPa) (Fig. 5c). Above 3 wt.% H₂O fragmentation depth decreases with increasing H₂O content. The effect of CO₂ on the fragmentation depth is different, such that fragmentation depth increases with increasing CO₂ content (Fig. 5f) over the complete range of values tested here, as was also highlighted in the excess CO₂ simulations above.

Role of external volatile sources on magma ascent dynamics.

The total volatile content in a magma chamber can vary via several mechanisms, including interaction with external sources, such as carbonate rocks, and assimilation of CO₂ in a closed system environment^{59,60} (Fig. 6). If gas cannot escape from the system, these interactions result in an increase not only in total volatile content, but also in chamber pressure. Magma chambers are not rigid bodies, so an increase in chamber pressure may also generate an increase in chamber volume (Fig. 6). According to Tait et al.⁶¹, the relative increase in chamber volume ΔV with respect to the initial volume V can be calculated as [Eq. 1]

$$\Delta V = \frac{3 \Delta P}{4 \mu_c} V, \quad (1)$$

where ΔP is the relative increase in chamber pressure and μ_c is the rigidity of the surrounding rock (here assumed to be 10 GPa, after Tait et al.⁶¹). Using the previous equation, and a mass balance calculation, we can compute the increase in both chamber pressure and volume produced by the addition of a given amount of water or carbon dioxide into the magma chamber. We then investigate the role of external volatile sources on magma ascent dynamics by performing numerical simulations considering an increase of either 1 wt.% H₂O or 1 wt.% CO₂ with respect to the reference values (Table 1) and calculating the resulting increase in both chamber pressure and volume. The main difference between the simulations presented in the sections above and the following

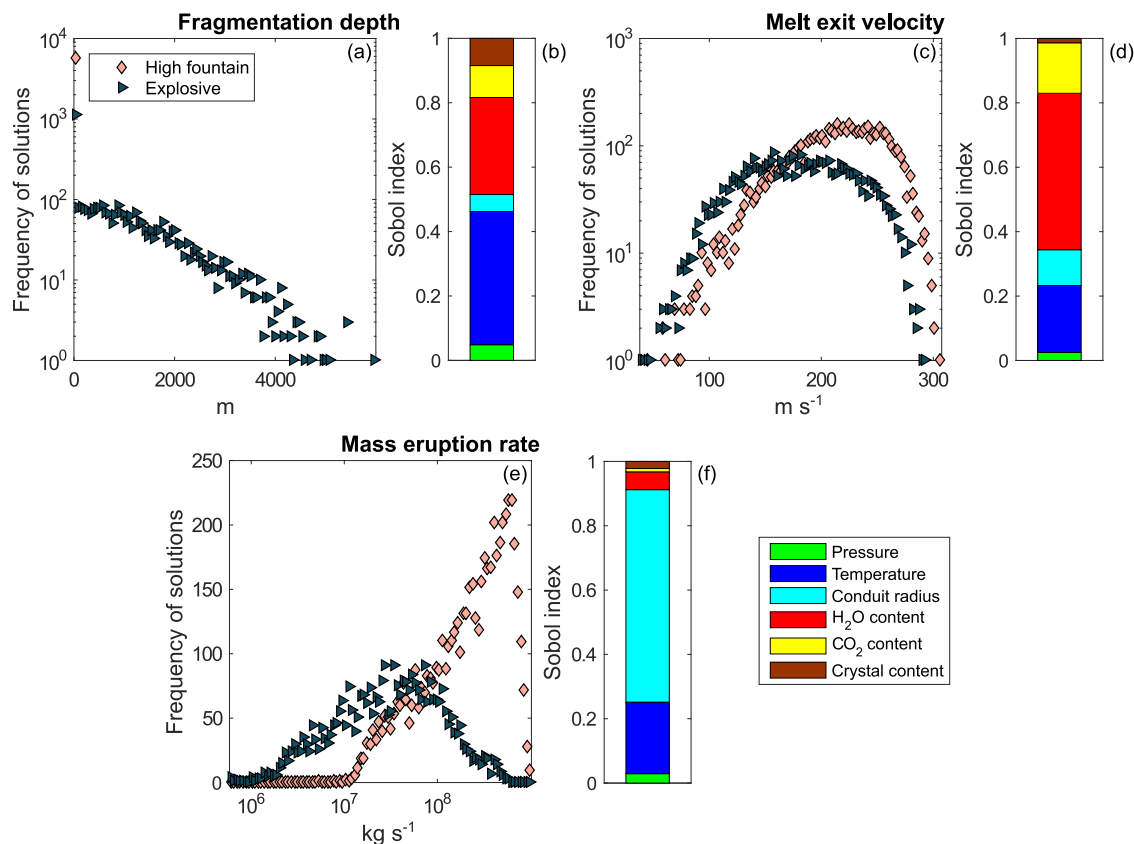


Fig. 4 Frequency of solutions as function of the investigated output parameters and the corresponding Sobol indexes resulting from the sensitivity analysis. We plot the number of solutions obtained from the sensitivity analysis as a function of selected output parameters and the corresponding Sobol indexes: (a, b) fragmentation depth; (c, d) melt exit velocity; (e, f) mass eruption rate. In contrast to what illustrated in Fig. 3, the sum of the frequencies here is variable, and is expressed as raw number (i.e. out of 10,000 runs). Explosive simulations are indicated with dark green triangles, whereas high fountains simulations are marked with pink diamonds.

analysis is that each of the previous simulations represents a single eruptive scenario, each with its own unique magmatic storage condition; whereas below the mass of magma (melt + crystal) remains constant across all simulations, while the pressure and volume of the magma chamber are adjusted to account for the increased mass of volatiles due to the interaction with an external source.

For our test case eruption, an increase of 1 wt.% H₂O or 1 wt.% CO₂ due to external sources produces an increase in chamber pressure of 31 or 69 MPa (Table 1 and Fig. 7a), and an increase in chamber volume of 0.2% or 0.5%, respectively. Notwithstanding the increase in total volatile content, the gas volume fraction at depth remains similar to the reference case (Fig. 7b), balanced by the increase in pressure. However, the ascent rates with the addition of 1 wt.% external volatiles are significantly higher than those of the reference case (Fig. 7c), and they are comparable to those calculated with 10 wt.% H₂O at a chamber pressure of 160 MPa (Fig. 2c). Similarly, MERs increase by about an order of magnitude with respect to the reference case (Fig. 7d), indicating that the addition of a small amount of external water or carbon dioxide at chamber depth can strongly affect the intensity of an eruption. Regarding the style of activity, the strong increase in velocity at depth precludes high strain-rates, and thus we observe a shift in style, from powerful explosive eruptions (reference solution) to lava fountaining (solutions with external volatiles).

Our results indicate that the increase in total volatiles due to interaction with external sources and the consequent increase in magma chamber pressure can have a strong impact on the magnitude of the eruption, ultimately culminating into a

transition in eruptive style from highly explosive behaviour to lava fountaining.

Conclusions

In conclusion, our numerical investigation indicates the fundamental role that volatiles play in controlling the ascent rate of basaltic magmas. We show that basaltic magmas with high water content ascend faster than the same magmas with lower water content, due to higher buoyancy and lower magma viscosity. Increasing CO₂ content increases viscosity, balancing higher buoyancy and leading to weak correlation between CO₂ content and magma ascent rate. However, when CO₂ is added to the closed system at chamber depth from an external source, such as due to an interaction with a carbonate rock, the increase in chamber pressure resulting from the addition of CO₂ produces sufficient driving force to strongly increase the MER.

Variation in volatile content can also affect the style of activity, potentially leading to a change in style from stronger to weaker explosive behaviour and vice versa. We show that, if exsolved volatiles are not able to decouple efficiently from the melt at shallow depths (<6 km), magma is more likely to fragment and produce highly explosive eruptions such as Plinian and sub-Plinian eruptions at low water content, due to higher magma viscosity. This is consistent with evidence from very powerful basaltic Plinian eruptions (such as Etna 122 BCE, Masaya Triple Layer, Tarawera 1886), which suggest that is possible to have highly explosive basaltic eruptions even with a low water content (<3 wt.%).

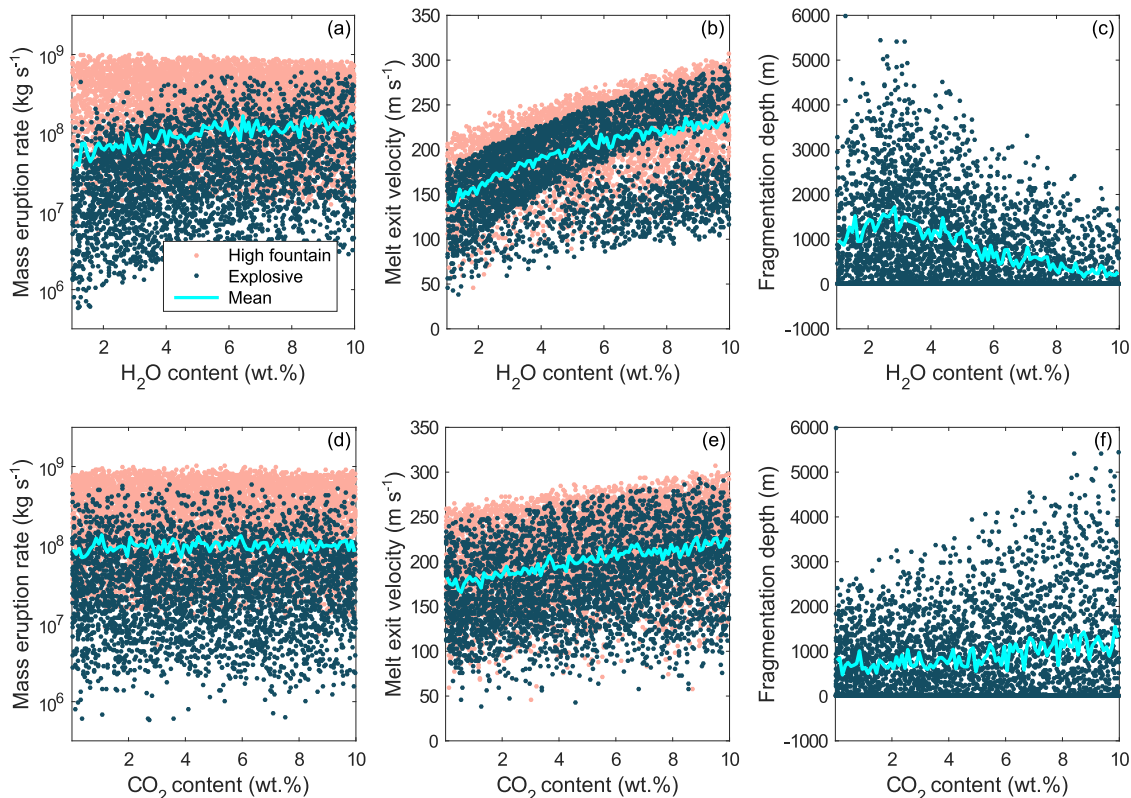


Fig. 5 Correlation plots of selected output parameters as function of each volatile content obtained from the sensitivity analysis. We illustrate the mass eruption rate as function of (a) H₂O and (d) CO₂, the melt/particle exit velocity as function of (b) H₂O and (e) CO₂, and the fragmentation depth as function of (c) H₂O and (f) CO₂. Each point (dark green for an explosive simulation and pink for a high fountains one) represents one of the 10,000 simulations from the sensitivity analysis. The cyan line is the mean of the output values at a given input value.

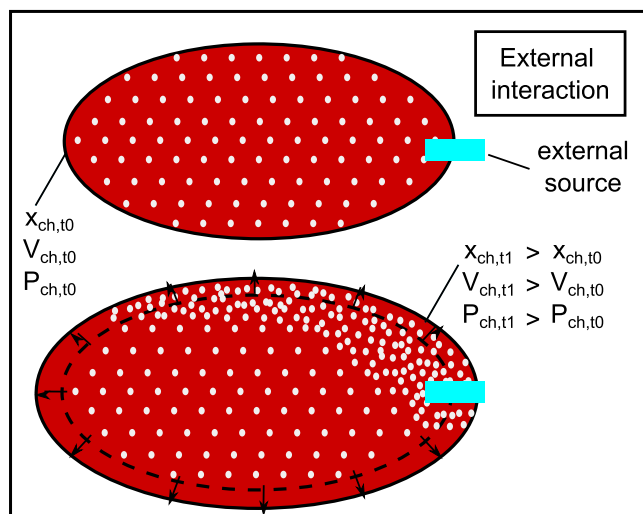


Fig. 6 Schematic representation of volatile accumulation due to interaction with an external source. As opposed to what illustrated in Fig. 1, we consider that, at time t_0 , the magma chamber comes in contact with an external source of volatiles (such as carbonate rocks), which will start to release volatiles within the chamber as exsolved bubbles. With time, due to the injection of these new bubbles into the magmatic system (which will accumulate close to the external source and towards the top of the chamber), the total volatile content within magma chamber will increase ($x_{ch,t1} > x_{ch,t0}$). Furthermore, this addition of new mass into the system will also produce an increase in magma chamber pressure ($P_{ch,t1} > P_{ch,t0}$) and a consequent increase in chamber volume ($V_{ch,t1} > V_{ch,t0}$).

Our most important result is that a variation in magmatic CO₂ volatile content has limited impact on the intensity or magnitude of a basaltic eruption. It is only when further volatiles from an external source (such as from carbonate rocks or ascending CO₂-rich bubbles) are added to a magma chamber, that the resulting increase of pressure is able to produce a significant change in MER.

It is important to highlight that our simulations describe the ascent dynamics of basaltic magmas ascending directly from a shallow source (<6 km), where CO₂ is already mostly exsolved, towards the surface. The presence of different proportions of CO₂ (either from internal or external sources) could change the dynamics deeper in the system, particularly where CO₂ initially exsolves, and H₂O is still mostly dissolved. In many cases, basaltic volcanoes have a shallow reservoir (2–6 km depth), such as Etna and Masaya^{55,62}. However, there is evidence of other volcanic systems where magma ascends directly from greater depths (>10 km), such as Sunset Crater³⁸. For this reason, the role of volatiles on the magma ascent dynamics for deep basaltic volcanic systems may be different from what we obtained for shallow systems, and thus requires further study.

Our work highlights how combining holistic numerical modelling of magma ascent with information from well-documented real eruptions can provide fundamental insights on the fluid and thermodynamics within the magmatic system, with potential future application to ongoing eruptions and associated risk management.

Methods

Governing equation of the 1D steady-state magma ascent model. Here we report the 1D steady-state model for magma ascent in a cylindrical conduit described by La Spina et al.⁴¹. During magma ascent several processes are taking place at the same time, such as temperature changes, viscosity evolution, non-ideal

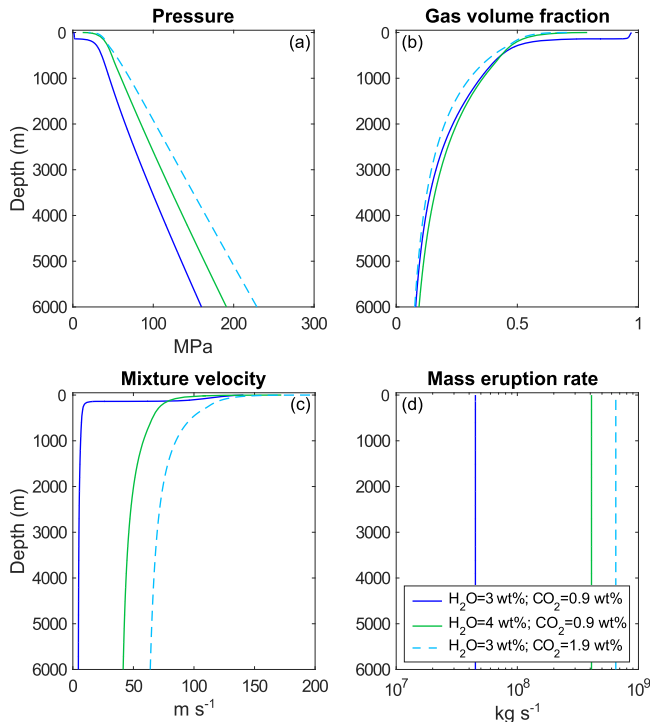


Fig. 7 Comparison of the numerical solutions for the reference and external volatile simulations. Evolution of (a) pressure, (b) exsolved gas volume fraction, (c) mixture velocity, and (d) mass eruption rate along the conduit obtained for the Etna 122 BCE reference case (blue solid lines) and for the external H₂O (green solid lines) and CO₂ (cyan dashed lines) cases. Compared to the first set of simulations, an increase in volatile content of 1 wt.% due to the interaction with an external volatile source results in magma chamber pressurisation and expansion, and ultimately in an increase in MER.

gas behaviour, outgassing and both disequilibrium crystallisation and exsolution. This model can solve for all these processes for each depth of the conduit at once.

The magmatic mixture is considered as a two-phase multicomponent compressible fluid. From the inlet of the conduit up to the fragmentation level, magma is assumed as a mixture of a liquid phase and a gas phase. The liquid phase (indicated by the subscript l) is made of a mixture of melt (subscript m), crystals (subscript c) and different dissolved gas components (subscript d). The gas phase (subscript g) represents bubbles of various exsolved gas components. If fragmentation occurs within the conduit, a transition from a bubbly-flow/permeable-flow regime towards a gas-ash flow regime is considered. Above that point up to the vent of the conduit magma is assumed to be a mixture of a dispersed particle phase (still indicated by subscript l) and a continuous gas phase.

To characterise and describe each of the two phases and each component within each phase we use several parameters, i.e. the volume fraction (α_k), mass density (ρ_k), mass fraction (x_k), velocity (u_k), specific internal energy (e_k), specific entropy (s_k), pressure (P_k) and temperature (T_k). We assume that all components within each phase have the same pressure, temperature and velocity (i.e. $P_m = P_c = P_d = P_l = P_g$ and $P_g = P_g$, and analogously for the temperature and velocity). Furthermore, the saturation constraints of $\alpha_l + \alpha_g = 1$ and $x_l + x_g = 1$ hold all along the conduit. Using the notations described previously, the mixture parameters can be defined as follows [Eq. 2]:

$$\begin{aligned} P &= \alpha_l P_l + \alpha_g P_g; \\ \rho &= \alpha_l \rho_l + \alpha_g \rho_g; \quad T = \alpha_l T_l + \alpha_g T_g; \\ x_l &= \frac{\alpha_l \rho_l}{\rho}; \quad u = x_l u_l + x_g u_g; \\ x_g &= \frac{\alpha_g \rho_g}{\rho}; \quad e = x_l e_l + x_g e_g; \\ & \quad s = x_l s_l + x_g s_g. \end{aligned} \quad (2)$$

The magma ascent model allows for relative motion and overpressure between the two phases of the magmatic mixture, which are governed by corresponding relaxation parameters (described afterwards). The temperature of the two phases, instead, is assumed to be in equilibrium (but not constant within the conduit) between the two phases.

The conservation equations for the mixture mass and momentum read as follow [Eqs.3 and 4]:

$$\frac{\partial \rho u}{\partial z} = 0, \quad (3)$$

$$\frac{\partial}{\partial z} \left[\sum_{k=l,g} \alpha_k \rho_k u_k^2 + \alpha_k P_k \right] = -\rho g - f_{D_l} \frac{\rho_l u_l^2}{4r} (1 - \phi_f) - f_{D_g} \frac{\rho_g u_g^2}{4r} \phi_f, \quad (4)$$

where g is the gravitational acceleration, r is the conduit radius (assumed to be fixed from depth up to the surface), ϕ_f is a binary variable indicating whether fragmentation is met within the conduit or not, and f_{D_l} and f_{D_g} are the Darcy–Weisbach friction factors, which are dependent on the conduit wall roughness and the Reynolds number (following the empirically-derived Moody diagram)⁶³.

The mixture energy equation is formulated following Zein et al. [Eq. 5]⁶⁴:

$$\frac{\partial}{\partial z} \left[\sum_{k=l,g} \alpha_k \rho_k u_k \left(e_k + \frac{P_k}{\rho_k} + \frac{u_k^2}{2} \right) \right] = -\rho g u. \quad (5)$$

The liquid volume fraction along the conduit is governed by the following transport equation [Eq. 6]:

$$\frac{\partial \rho \alpha_l}{\partial z} = -\frac{1}{\tau^{(p)}} (P_g - P_l). \quad (6)$$

The relaxation parameter $\tau^{(p)}$ ($m^2 s^{-1}$) defines the overpressure between gas and liquid phase. Following La Spina et al.⁴¹, it is reasonable to assume (for basaltic magmas) pressure equilibrium between the two phases, obtained by setting $\tau^{(p)} = 10^{-5} m^2 s^{-1}$.

The following partial differential equations are adopted to describe each exsolved gas component and the corresponding dissolved contents [Eqs. 7 and 8]:

$$\frac{\partial \alpha_i \rho_{g_i} u_g}{\partial z} = \frac{1}{\tau^{(e)}} \left(x_{d_i}^{md} - x_{d_i}^{md,eq} \right) \left(\alpha_l \rho_l - \sum_j \alpha_l \rho_c \beta_j \right), \quad (7)$$

$$\frac{\partial}{\partial z} \left(\rho x_{d_i}^{md} u_l \right) = -\frac{1}{\tau^{(e)}} \left(x_{d_i}^{md} - x_{d_i}^{md,eq} \right) \left(\alpha_l \rho_l - \sum_j \alpha_l \rho_c \beta_j \right), \quad (8)$$

where $x_{d_i}^{md}$ is the mass fraction of the dissolved gas phase i , while $x_{d_i}^{md,eq}$ is the same parameter but at equilibrium conditions. In these equations, the exsolution rate is controlled by the relaxation parameter $\tau^{(e)}$ (s). This characteristic time for basaltic magmas has not been constrained by experimental data, thus, following La Spina et al.³⁹, as a first order approximation we consider disequilibrium exsolution assuming a constant characteristic time $\tau^{(e)} = 1$ s.

The evolution of volume fractions of each crystal component within the conduit are governed by the following transport equation [Eq. 9]:

$$\frac{\partial}{\partial z} (\alpha_l \rho_c \beta_j u_l) = -\frac{1}{\tau^{(c)}} \alpha_l \rho_c (\beta_j - \beta_j^{eq}). \quad (9)$$

Here β_j is the volume fraction of the crystal component j while β_j^{eq} is the same physical quantity at equilibrium. As for exsolution of gas, the crystallisation rate is governed by the characteristic time $\tau^{(c)}$ (s). Following Arzilli et al.³¹, the disequilibrium crystallisation is taken into account assuming a constant characteristic time $\tau^{(c)} = 10$ s.

Finally, the relative motion between the two phases is controlled by the following partial differential equation [Eq. 10]:

$$\begin{aligned} \frac{\partial}{\partial z} \left[\frac{u_l^2}{2} - \frac{u_g^2}{2} + e_l + \frac{P_l}{\rho_l} - e_g - \frac{P_g}{\rho_g} - (s_l - s_g) T \right] = \\ -\frac{1}{\tau^{(r)}} \frac{\rho}{\rho_l \rho_g} (u_l - u_g) - f_{D_l} \frac{u_l^2}{4\alpha_l r} (1 - \phi_f) + f_{D_g} \frac{u_g^2}{4\alpha_g r} \phi_f. \end{aligned} \quad (10)$$

The degree of decoupling between the gas and the liquid phase is governed by a relaxation parameter $\tau^{(r)}$ ($kg^{-1} m^3 s$). A detailed description of how $\tau^{(r)}$ is calculated within the conduit can be found afterwards.

Constitutive equations for the Etna 122 BCE Plinian eruption. To simulate the magma ascent dynamics of the Etna 122 BCE Plinian eruption we adopted specific constitutive equations, such as rheological, crystallisation, wall friction, outgassing, fragmentation, and solubility models. Most of these equations have been illustrated in previous works^{28,31,40,41}. For completeness, we report below the constitutive equations adopted in this work.

The viscosity of the liquid phase (i.e. magma viscosity) is calculated as follows [Eq. 11]:

$$\mu_l = \mu_{melt} \cdot \theta_c, \quad (11)$$

where μ_{melt} is the viscosity of the bubble-free, crystal-free liquid phase, and θ_c is a factor which increases viscosity due to the presence of crystals⁶⁵. The viscosity of the bubble-free, crystal-free melt is computed using the following relationship⁶⁶, based on the Vogel–Fulcher–Tammann equation [Eq.12]:

$$\log(\mu_{melt}) = A + \frac{B(y, x_{d_{H_2O}}^{md})}{T - C(y, x_{d_{H_2O}}^{md})}. \quad (12)$$

In Eq. (12), the melt viscosity is expressed in Pa s, and temperature of the melt is expressed in Kelvin. The parameter A represents the logarithmic value of the

viscosity at infinite temperature. This parameter is assumed to be constant for all melts ($A = -4.5$). The parameters B and C , instead, are functions of the melt composition γ and of the dissolved water content $x_{d_{H_2O}}^{md}$. In this work, we used the average melt inclusion composition for Etna 122 BCE from Del Carlo and Pompilio⁴ (Supplementary Table 1). As crystallisation occurs within the conduit, viscosity is increased according to the model illustrated by Costa et al. [Eqs. 13–15]⁶⁷:

$$\theta = \frac{1 + \varphi^\delta}{[1 - F(\varphi, \xi, \gamma)]^{\beta\phi^*}}, \quad (13)$$

where

$$F = (1 - \xi) \operatorname{erf} \left[\frac{\sqrt{\pi}}{2(1 - \xi)} \varphi(1 + \varphi^\gamma) \right], \quad (14)$$

$$\varphi = \frac{\left(\sum_{j=1}^{n_c} x_{c_j}^1 \right)}{\phi^*}. \quad (15)$$

The fitting parameters B , δ , ξ , γ and ϕ^* chosen for this work are the same used in Vona et al.⁶⁸: $B = 2.8$, $\delta = 0.0327$, $\gamma = 0.84$, $\delta = 13 - \gamma$, and $\phi^* = 0.274$.

The crystallisation model adopted here has been proposed by La Spina et al.²⁹. In this work, we consider the three different major crystal components in basaltic magmas: plagioclase, olivine and pyroxene. No fractional crystallisation is assumed to occur during magma ascent, which means that crystals stay coupled with the melt. For a better modelling of crystal nucleation and growth, we also assume that the equilibrium crystal contents are functions of temperature, pressure and dissolved water content. With these assumptions and following La Spina et al.²⁹, the equilibrium mass fraction $x_{c_j}^{1,eq}$ of crystal phase j is computed using the polynomial function [Eq. 16]

$$x_{c_j}^{1,eq}(P^*, T^*, x_d^*) = \zeta_{j,1}(P^*)^2 + \zeta_{j,2}(T^*)^2 + \zeta_{j,3}(x_d^*)^2 + \zeta_{j,4}(P^*)(T^*) + \zeta_{j,5}(T^*)(x_d^*) + \zeta_{j,6}(x_d^*)(P^*) + \zeta_{j,7}(P^*) + \zeta_{j,8}(T^*) + \zeta_{j,9}(x_d^*) + \zeta_{j,10}, \quad (16)$$

where P^* is the magma pressure (expressed in bars), T^* is the temperature (expressed in Celsius degrees) and x_d^* is the dissolved water concentration (expressed in weight percent). From $x_{c_j}^{1,eq}$, the equilibrium crystal volume fraction β_j^{eq} can be computed using the relation [Eq. 17]

$$\beta_j^{eq} = \frac{\rho_j x_{c_j}^{1,eq}}{\rho_c}. \quad (17)$$

By fitting the Eq. (16) over a large range of data obtained at different pressures, temperatures and water contents with alphaMELTS⁶⁹, a command line version of MELTS⁷⁰, it is possible to calculate the parameters $\zeta_{j,i}$. The melt compositions used for the fitting Etna 122 BCE crystallisation model is reported in Supplementary Table 1, whereas the fitting coefficients for each crystal component are reported in Supplementary Table 2.

Following La Spina et al.⁴⁰, we considered both laminar and turbulent regimes, according to the Reynolds number of the liquid phase (Re) calculated as follows [Eq. 18]:

$$Re = \frac{\rho_l u_l 2r}{\mu_l}. \quad (18)$$

For Reynolds numbers smaller than 2000, the flow is assumed laminar, and the friction factor for the liquid phase f_{D_l} is calculated using the widely used Hagen–Poiseuille’s law [Eq. 19]:

$$f_{D_l}^{laminar} = \frac{64}{Re}. \quad (19)$$

When $Re > 3000$, the friction factor for fully-developed turbulent flow is approximated following Fang et al. [Eq. 20]⁷¹:

$$f_{D_l}^{turbulent} = 1.613 \left[\ln \left(0.23Rr^{1.1007} - \frac{60.525}{Re^{1.1105}} + \frac{56.291}{Re^{1.0712}} \right) \right]^{-2}. \quad (20)$$

where Rr is the relative roughness of the pipe, assumed to be $Rr = 0.05$ in agreement with La Spina et al.⁴⁰. For Reynolds number between 2000 and 3000, a transitional regime is considered, computing the friction factor as a linear interpolation between $f_{D_l}^{laminar}$ and $f_{D_l}^{turbulent}$. Above the fragmentation level, the friction factor for the gas phase f_{D_g} is set to 0.03 as done by Degruyter et al.⁷².

The transition between effusive and explosive eruptions is controlled by the efficiency of gas escape during magma ascent^{73,74}. If gas is able to decouple efficiently from magma, an effusive eruption occurs. On the other hand, a strong coupling between gas and melt may lead to magma fragmentation and explosive eruption. Therefore, a correct modellization of relative motion between gas and melt is crucial for a correct description of eruptive style transitions. Here we consider only vertical gas loss, whereas lateral gas escape is not taken into account.

There are several regimes describing gas flow in a liquid mixture: a bubbly-flow regime (where non-interacting separated bubbles ascend uniformly distributed in the liquid), a slug flow regime (in which bubbles coalesce in a few large bubbles

with diameter comparable to the conduit diameter), an annular flow regime (where liquid forms a sort of annular ring at the conduit walls, with gas ascending along the center of the conduit), a permeable gas flow regime (in which gas flows through interconnected pathways within the melt)^{7,28,75–77}. Following La Spina et al.²⁸ and Degruyter et al.⁷², below fragmentation depth we assumed a permeable gas low regime, whereas above the fragmentation level we used the model adopted by Yoshida and Koyaguchi⁷⁸.

The relative velocity between the two phases is thus governed by the velocity relaxation rate $\tau^{(i)}$ ($\text{kg}^{-1}\text{m}^3\text{s}$), which can be expressed in the following form [Eq. 21]:

$$\tau^{(i)} = \left[\left(\frac{\mu_g}{k_v} + \frac{\rho_g |u_l - u_g|}{k_i} \right)^{(1-\phi_i)} \cdot \left(\frac{3C_D}{8r_a} \rho_g |u_l - u_g| \right)^{\phi_i} \right]^{-1}. \quad (21)$$

Here, C_D is a drag coefficient, r_a is the average size of the fragmented magma particles, and k_v and k_i are viscous and inertial permeability, respectively. Both permeabilities can be calculated following Degruyter et al. [Eqs. 22–23]⁷²:

$$k_v = \frac{(f_{ib} r_b)^2}{8} \alpha_g^m \quad (22)$$

$$k_i = \frac{f_{ib} r_b}{f_0} \alpha_g^{\frac{1+3m}{2}} \quad (23)$$

where f_{ib} is the throat-bubble size ratio, m is the tortuosity factor, f_0 is a friction coefficient, and r_b is the average bubble size calculated as [Eq. 24]

$$r_b = \left(\frac{\alpha_g}{\frac{4\pi}{3} N_d \alpha_l} \right)^{\frac{1}{3}}. \quad (24)$$

For our simulations, in agreement with La Spina et al.⁴¹, we used the following values: $C_D = 0.8$, $r_a = 10^{-3}$ m, $f_{ib} = 0.8$, $m = 5$, $N_d = 10^{13}$ and $f_0 = 10^{-5}$.

Magma fragmentation is assumed to occur when the ratio between the Maxwell relaxation timescale (λ_r) and the timescale of deformation (λ_d) is greater than 0.01. By defining the Deborah number (De) as the ratio between the Maxwell relaxation timescale and the timescale of deformation, the following fragmentation criterion for magmatic mixture can be defined (brittle criterion) [Eq. 25]:

$$De = \frac{\lambda_r}{\lambda_d} = \frac{\left(\frac{\mu_l}{G_\infty} \right)}{\left(\frac{1}{\dot{\gamma}} \right)} = \frac{\mu_l \dot{\gamma}}{G_\infty} > 0.01. \quad (25)$$

Here, μ_l is the magma bulk viscosity (Eq. 11), $\dot{\gamma}$ is the strain rate and G_∞ is the unrelaxed shear modulus at infinite frequency of the magma⁷⁹, which for a basaltic magma can be assumed $G_\infty = 10^{10}$ Pa.

In comparison with previous works^{28,31,40,41}, here we implemented new solubility models for H_2O and CO_2 based on the work done in Allison et al.³⁷. The equilibrium dissolved water content as a function of water fugacity has been modelled following the results for Etna presented in Lesne et al. [Eq. 26]²¹:

$$x_{d_{H_2O}}^{md,eq} = 0.01 \cdot \left(\frac{\hat{f}_{H_2O}}{104.98} \right)^{\frac{1}{183}}, \quad (26)$$

where $\hat{f}_{H_2O} = f_{H_2O}/I_{bar}$ is the non-dimensional water fugacity, f_{H_2O} is the water fugacity expressed in bars, and I_{bar} is the unity in bars. Following Holloway and Blank⁸⁰ and La Spina et al.⁴⁰ we approximate water fugacity as [Eq. 27]:

$$f_{H_2O} = 0.9823(P_{H_2O}), \quad (27)$$

where P_{H_2O} is the partial pressure of water expressed in bars. The partial pressure of water is calculated as $P_{H_2O} = \alpha_{g_{H_2O}} P_g / \alpha_g$, where P_g is the pressure of the gas phase (expressed in bars), and $\alpha_{g_{H_2O}}$ and α_g are the volume fractions of the exsolved water and of the total gas phase, respectively²⁹. Since we only consider two gas species, the following saturation constraint holds: $\alpha_g = \alpha_{g_{H_2O}} + \alpha_{g_{CO_2}}$.

The equilibrium dissolved CO_2 content, instead, has been modelled as a function of carbon dioxide fugacity, which, following Allison et al.³⁷, reads as follow [Eq. 28]:

$$x_{d_{CO_2}}^{md,eq} = 2.831 \times 10^{-6} (\hat{f}_{CO_2})^{0.797}. \quad (28)$$

Here, $\hat{f}_{CO_2} = f_{CO_2}/I_{bar}$ is a non-dimensional variable and f_{CO_2} is the fugacity of CO_2 expressed in bars. Again, following Holloway and Blank⁸⁰ and La Spina et al.⁴⁰, carbon dioxide fugacity can be approximated with a 6th order polynomial [Eq. 29]:

$$\hat{f}_{CO_2} = -(b_6 \hat{P}_{CO_2})^6 + (b_5 \hat{P}_{CO_2})^5 + (b_4 \hat{P}_{CO_2})^4 + (b_3 \hat{P}_{CO_2})^3 + (b_2 \hat{P}_{CO_2})^2 + (b_1 \hat{P}_{CO_2}) + b_0, \quad (29)$$

where $\hat{P}_{CO_2} = P_{CO_2}/I_{bar}$ is the non-dimensional partial pressure of carbon dioxide, $P_{CO_2} = \alpha_{g_{CO_2}} P_g / \alpha_g$ is the partial pressure expressed in bars, $b_6 = 6.62 \times 10^{-4}$, $b_5 = 9.49 \times 10^{-4}$, $b_4 = 4.63 \times 10^{-4}$, $b_3 = 3.31 \times 10^{-3}$, $b_2 = 1.46 \times 10^{-2}$, $b_1 = 0.999999857$, and $b_0 = 2.32 \times 10^{-6}$. Since the saturation constraint $\alpha_g = \alpha_{g_{H_2O}} + \alpha_{g_{CO_2}}$ holds, we also have that $P_g = P_{H_2O} + P_{CO_2}$.

Equations of state and boundary conditions. In order to close the system of governing and constitutive equations, equations of state for melt, crystals, dissolved and exsolved gases (as function of density and temperature) have to be defined.

For the exsolved gas components, we adopted the Van der Waals non-ideal gas equations of state [Eq. 30]²⁹:

$$\begin{cases} e_{g_i}(\rho_{g_i}, T) = c_{v,g_i} T - a_{g_i} \rho_{g_i} + \bar{e}_{g_i}, \\ P_{g_i}(\rho_{g_i}, T) = c_{v,g_i} (\gamma_{g_i} - 1) T \frac{\rho_{g_i}}{1 - b_{g_i} \rho_{g_i}} - a_{g_i} \rho_{g_i}^2, \\ s_{g_i}(\rho_{g_i}, T) = c_{v,g_i} \log \left[\frac{T}{T_{0,g_i}} \left(\frac{\rho_{0,g_i}}{\rho_{g_i}} \cdot (1 - b_{g_i} \rho_{g_i}) \right)^{(\gamma_{g_i} - 1)} \right], \\ C_{g_i}(\rho_{g_i}, T) = \sqrt{\frac{c_{v,g_i} (\gamma_{g_i} - 1) \gamma_{g_i} T}{(1 - b_{g_i} \rho_{g_i})^2}} - 2a_{g_i} \rho_{g_i} \end{cases} \quad (30)$$

for $i = 1, \dots, n_g$. Here \bar{e} is a constant parameter representing the formation energy of the fluid, c_v is the specific heat capacity at constant volume, γ is the adiabatic exponent, ρ_0 , P_0 , T_0 , s_0 and C_0 are respectively the density, pressure, temperature, specific entropy and speed of sound at a reference state. The coefficients a_{g_i} and b_{g_i} are defined as [Eq.31]

$$a_{g_i} = \frac{27 c_{v,g_i}^2 (\gamma_{g_i} - 1)^2 T_{c,g_i}^2}{64 P_{c,g_i}}, \quad b_{g_i} = \frac{1 c_{v,g_i} (\gamma_{g_i} - 1) T_{c,g_i}}{8 P_{c,g_i}}, \quad (31)$$

where P_{c,g_i} and T_{c,g_i} are respectively the critical pressure and temperature of the gas component g_i .

A linearised version of the Mie–Grüneisen equations of state has been adopted for melt and crystals phases [Eq. 32]^{81,82}:

$$\begin{cases} e_k(\rho_k, T) = \bar{e}_k + c_{v,k} T + \frac{\rho_{0,k} C_{0,k}^2 - \gamma_k P_{0,k}}{\gamma_k \rho_k}, \\ P_k(\rho_k, T) = c_{v,k} (\gamma_k - 1) \rho_k T - \frac{\rho_{0,k} C_{0,k}^2 - \gamma_k P_{0,k}}{\gamma_k}, \\ s_k(\rho_k, T) = s_{0,k} + c_{v,k} \ln \left[\frac{T}{T_{0,k}} \left(\frac{\rho_{0,k}}{\rho_k} \right)^{\gamma_k - 1} \right], \\ C_k(\rho_k, T) = C_{0,k} \sqrt{\left(\frac{\rho_k}{\rho_{0,k}} \right)^{\gamma_k - 1} \exp \left(\frac{s_k(\rho_k, T) - s_{0,k}}{c_{v,k}} \right)}, \end{cases} \quad (32)$$

where $k = m, c_j$ for $j = 1, \dots, n_c$.

To calculate the numerical solution of the 1D steady-state model for magma ascent, boundary conditions have to be defined. At the inlet of the conduit we set the initial pressure, temperature, total content of volatiles (water and carbon dioxide), and the initial crystal content (phenocryst content). At the vent of the conduit, instead, two boundary conditions are allowed: atmospheric pressure (0.1 MPa) and/or choked flow condition. The choked flow condition is met when the mixture velocity is equal to the speed of sound of the mixture (i.e. when the Mach number is equal to 1). In this case, the pressure at the vent of the conduit may be greater than the atmospheric pressure. The speed of sound of the mixture is calculated using the following equation [Eq. 33]:

$$C = \frac{1}{\sqrt{K\rho}}, \quad (33)$$

where $K = \alpha_1 K_1 + \alpha_g K_g$ is the compressibility of the mixture.

The numerical solutions are calculated integrating all the system of partial differential equations coupled with appropriate constitutive equations, equations of state and boundary conditions, from the inlet of the conduit up to the vent. Specifically, the numerical solution is computed using a shooting technique, which consists of searching for the initial magma ascent velocity that satisfy the boundary conditions at the vent of the conduit (i.e. atmospheric pressure or choked flow condition)⁸³. Furthermore, when the solution begins to be highly non-linear the numerical solver refines automatically the step-size of integration. With a decrease in step-size, however, the approximation of the derivatives may introduce truncation errors due subtractive cancellations in the approximations, causing instabilities and difficulties in converging to the correct solution. To overcome this problem, we used a reliable method for calculating the derivatives, which is based on complex functions. This has been described in La Spina et al.⁸². By adopting the complex step derivative approximation, the step-size of integration can be as small as required, with no further numerical errors introduced in the solutions.

Data availability

The authors declare that all other relevant data supporting the findings of this study are included in the paper, in the Supplementary Information, and in the Supplementary Data 1 and 2. Model outputs resulting from the sensitivity analysis of this study are available from the corresponding author upon request.

Code availability

The magma ascent model used in this study has been adapted from the MAMMA model available on GitHub: <https://github.com/demichie/MAMMA>. The version of the MAMMA model used to obtain the numerical results of this work⁸⁴ is available here: <https://doi.org/10.6084/m9.figshare.19361981>.

Received: 26 October 2021; Accepted: 16 June 2022;

Published online: 06 July 2022

References

- Sparks, R. S. J. The dynamics of bubble formation and growth in magmas: a review and analysis. *J. Volcanol. Geothermal Res.* **3**, 1–37 (1978).
- Roggensack, K., Hervig, R. L., McKnight, S. B. & Williams, S. N. Explosive basaltic volcanism from Cerro Negro volcano: influence of volatiles on eruptive style. *Science* **277**, 1639 (1997).
- Cashman, K. V. Volatile controls on magma ascent and eruption. In *The state of the planet: Frontiers and challenges in geophysics. American Geophysical Union Geophysical Monograph 150*, (eds Sparks, R. S. J. & Hawkesworth, C. J.), 109–124, <https://doi.org/10.1029/150GM10> (2004).
- Del Carlo, P. & Pompilio, M. The relationship between volatile content and the eruptive style of basaltic magma: the Etna case. *Ann. Geophys.* **47**, <https://doi.org/10.4401/ag-4402> (2004).
- Spilliaert, N., Allard, P., Métrich, N. & Sobolev, A. V. Melt inclusion record of the conditions of ascent, degassing, and extrusion of volatile-rich alkali basalt during the powerful 2002 flank eruption of Mount Etna (Italy). *J. Geophys. Res.* **111**, <https://doi.org/10.1029/2005jb003934> (2006).
- Johnson, E. R., Wallace, P. J., Cashman, K. V. & Granados, H. D. Degassing of volatiles (H₂O, CO₂, S, Cl) during ascent, crystallization, and eruption at mafic monogenetic volcanoes in central Mexico. *J. Volcanol. Geothermal Res.* **197**, 225–238 (2010).
- Gonnermann, H. M. & Manga, M. Dynamics of magma ascent in the volcanic conduit. In *Modeling Volcanic Processes*, (eds Fagents, S. A., Gregg, T. K. P. and Lopes, R. M. C.) 55–84 (Cambridge Univ Press, 2013) <https://doi.org/10.1017/cbo9781139021562.004>.
- Wallace, P. J., Plank, T., Edmonds, M. & Hauri, E. H. Volatiles in magmas. In *The encyclopedia of volcanoes*. 163–183 (Elsevier, 2015) <https://doi.org/10.1016/b978-0-12-385938-9.00007-9>.
- Edmonds, M. & Wallace, P. J. Volatiles and Exsolved Vapor in Volcanic Systems. *Elements* **13**, 29–34 (2017).
- Petrelli, M. et al. Timescales of water accumulation in magmas and implications for short warning times of explosive eruptions. *Nat. Commun.* **9**, 770 (2018).
- Anderson, A. T. Some basaltic and andesitic gases. *Rev. Geophys.* **13**, 37 (1975).
- Burton, M., Allard, P., Muré, F. & La Spina, A. Magmatic gas composition reveals the source depth of slug-driven Strombolian explosive activity. *Science* **317**, 227–230 (2007).
- Moune, S., Sigmarsson, O., Thordarson, T. & Gauthier, P.-J. Recent volatile evolution in the magmatic system of Hekla volcano, Iceland. *Earth Planetary Sci. Lett.* **255**, 373–389 (2007).
- Allard, P. et al. Crater gas emissions and the magma feeding system of Stromboli volcano. *The Stromboli Volcano: An Integrated Study of the 2002–2003 Eruption*, 65–80, <https://doi.org/10.1029/182gm07> (2008).
- Métrich, N. & Wallace, P. J. Volatile Abundances in Basaltic Magmas and Their Degassing Paths Tracked by Melt Inclusions. *Rev. Mineral Geochem.* **69**, 363–402 (2008).
- Aiuppa, A. et al. Unusually large magmatic CO₂ gas emissions prior to a basaltic paroxysm. *Geophys. Res. Lett.* **37**, <https://doi.org/10.1029/2010gl043837> (2010).
- Fiege, A., Vetere, F., Iezzi, G., Simon, A. & Holtz, F. The roles of decompression rate and volatiles (H₂O+Cl±CO₂±S) on crystallization in (trachy-) basaltic magma. *Chem. Geol.* **411**, 310–322 (2015).
- Caricchi, L., Sheldrake, T. E. & Blundy, J. Modulation of magmatic processes by CO₂ flushing. *Earth Planetary Sci. Lett.* **491**, 160–171 (2018).
- Pistone, M., Caricchi, L. & Ulmer, P. CO₂ favours the accumulation of excess fluids in felsic magmas. *Terra Nova*, **9**, <https://doi.org/10.1111/ter.12496> (2020).
- Wilson, L., Sparks, R. S. J. & Walker, G. P. L. Explosive volcanic eruptions IV. The control of magma properties and conduit geometry on eruption column behavior. *Geophys. J. Royal Astronomical Soc.* **63**, 117–148, <https://doi.org/10.1111/j.1365-246X.1980.tb02613.x> (1980).
- Lesne, P., Scailliet, B., Pichavant, M., Iacono-Marziano, G. & Beny, J.-M. The H₂O solubility of alkali basaltic melts: an experimental study. *Contributions Mineral. Petrol.* **162**, 133–151 (2011).
- Vergnolle, S. & Gaudemer, Y. From reservoirs and conduits to the surface: review of role of bubbles in driving basaltic eruptions. In *Hawaiian Volcanoes: From Source to Surface. American Geophysical Union Geophysical Monograph 208* (eds Carey, R., Cayol, V., Poland, M. & Weis, D.), 289–322, <https://doi.org/10.1002/9781118872079.ch14> (2015).
- Moore, G., Vennemann, T. & Carmichael, I. S. E. An empirical model for the solubility of H₂O in magmas to 3 kilobars. *Am. Mineralogist* **83**, 36–42 (1998).

24. Applegarth, L. J., Tuffen, H., James, M. R. & Pinkerton, H. Degassing-driven crystallisation in basalts. *Earth-Sci. Rev.* **116**, 1–16 (2013).
25. Edmonds, M. & Woods, A. W. Exsolved volatiles in magma reservoirs. *J. Volcanol. Geothermal Res.* **368**, 13–30 (2018).
26. Burton, M. R., Mader, H. M. & Polacci, M. The role of gas percolation in quiescent degassing of persistently active basaltic volcanoes. *Earth Planetary Sci. Lett.* **264**, 46–60 (2007).
27. Houghton, B. F. & Gonnermann, H. M. Basaltic explosive volcanism: constraints from deposits and models. *Chemie der Erde-Geochem.* **68**, 117–140 (2008).
28. La Spina, G., Polacci, M., Burton, M. & de' Michieli Vitturi, M. Numerical investigation of permeability models for low viscosity magmas: application to the 2007 Stromboli effusive eruption. *Earth Planetary Sci. Lett.* **473**, 279–290 (2017).
29. La Spina, G., Burton, M. & de' Michieli Vitturi, M. Temperature evolution during magma ascent in basaltic effusive eruptions: A numerical application to Stromboli volcano. *Earth Planetary Sci. Lett.* **426**, 89–100 (2015).
30. Mader, H. M., Llewellyn, E. W. & Mueller, S. P. The rheology of two-phase magmas: a review and analysis. *J. Volcanol. Geothermal Res.* **257**, 135–158 (2013).
31. Arzilli, F. et al. Magma fragmentation in highly explosive basaltic eruptions induced by rapid crystallization. *Nat. Geosci.* **10**, <https://doi.org/10.1038/s41561-019-0468-6> (2019).
32. Sparks, R. S. J. & Pinkerton, H. Effect of degassing on rheology of basaltic lava. *Nature* **276**, 385–386 (1978).
33. Starostin, A. B., Barmin, A. A. & Melnik, O. E. A transient model for explosive and phreatomagmatic eruptions. *J. Volcanol. Geothermal Res.* **143**, 133–151 (2005).
34. Allard, P. A CO₂-rich gas trigger of explosive paroxysms at Stromboli basaltic volcano, Italy. *J. Volcanol. Geothermal Res.* **189**, 363–374 (2010).
35. Aiuppa, A. et al. First observational evidence for the CO₂-driven origin of Stromboli's major explosions. *Solid Earth*, <https://doi.org/10.5194/se-2-135-2011> (2011).
36. Helo, C., Longpré, M.-A., Shimizu, N., Clague, D. A. & Stix, J. Explosive eruptions at mid-ocean ridges driven by CO₂-rich magmas. *Nat. Geosci.* **4**, 260–263 (2011).
37. Allison, C. M., Roggensack, K. & Clarke, A. B. H₂O–CO₂ solubility in alkali-rich mafic magmas: new experiments at mid-crustal pressures. *Contrib. Mineral. Petrol.* **174**, <https://doi.org/10.1007/s00410-019-1592-4> (2019).
38. Allison, C. M., Roggensack, K. & Clarke, A. B. Highly explosive basaltic eruptions driven by CO₂ exsolution. *Nat. Commun.* **12**, <https://doi.org/10.1038/s41467-020-20354-2> (2021).
39. La Spina, G., Burton, M., de' Michieli Vitturi, M. & Arzilli, F. Role of syn-eruptive plagioclase disequilibrium crystallization in basaltic magma ascent dynamics. *Nat. Commun.* **7**, 13402 (2016).
40. La Spina, G. et al. Conduit dynamics of highly explosive basaltic eruptions: The 1085 CE Sunset Crater sub-Plinian events. *J. Volcanol. Geother. Res.* **387**, 106658 (2019).
41. La Spina, G. et al. Explosivity of basaltic lava fountains is controlled by magma rheology, ascent rate and outgassing. *Earth Planetary Sci. Lett.* **553**, 116658 (2021).
42. Aravena, A., de' Michieli Vitturi, M., Cioni, R. & Neri, A. Physical constraints for effective magma-water interaction along volcanic conduits during silicic explosive eruptions. *Geology* <https://doi.org/10.1130/g45065.1> (2018).
43. Aravena, A. et al. Effusion Rate Evolution During Small-Volcanic Basaltic Eruptions: Insights From Numerical Modeling. *J. Geophys. Res.: Solid Earth*, **125**, <https://doi.org/10.1029/2019jb019301> (2020).
44. Carr, B. B., Clarke, A. B. & de' Michieli Vitturi, M. Earthquake induced variations in extrusion rate: A numerical modeling approach to the 2006 eruption of Merapi Volcano (Indonesia). *Earth Planetary Sci. Lett.* **482**, 377–387 (2018).
45. Carr, B. B., Clarke, A. B. & de' Michieli Vitturi, M. Volcanic conduit controls on effusive-explosive transitions and the 2010 eruption of Merapi Volcano (Indonesia). *J. Volcanol. Geothermal Res.* **392**, 106767 (2020).
46. Coltelli, M., Del Carlo, P. & Vezzoli, L. Discovery of a Plinian basaltic eruption of Roman age at Etna volcano, Italy. *Geology* **26**, 1095–1098 (1998).
47. Houghton, B. F. et al. The influence of conduit processes on changes in style of basaltic Plinian eruptions: Tarawera 1886 and Etna 122 BC. *J. Volcanol. Geother. Res.* **137**, 1–14 (2004).
48. Sable, J. E., Houghton, B. F., Del Carlo, P. & Coltelli, M. Changing conditions of magma ascent and fragmentation during the Etna 122 BC basaltic Plinian eruption: Evidence from clast microtextures. *J. Volcanol. Geother. Res.* **158**, 333–354 (2006).
49. Costantini, L., Houghton, B. F. & Bonadonna, C. Constraints on eruption dynamics of basaltic explosive activity derived from chemical and microtextural study: the example of the Fontana Lapilli Plinian eruption, Nicaragua. *J. Volcanol. Geother. Res.* **189**, 207–224 (2010).
50. Campagnola, S., Romano, C., Mastin, L. G. & Vona, A. Confort 15 model of conduit dynamics: applications to Pantelleria Green Tuff and Etna 122 BC eruptions. *Contrib. Mineral. Petrol.* **171**, 60 (2016).
51. Pardini, F., Burton, M., Arzilli, F., Spina, G. L. & Polacci, M. SO₂ emissions, plume heights and magmatic processes inferred from satellite data: The 2015 Calbuco eruptions. *J. Volcanol. Geother. Res.* **361**, 12–24 (2018).
52. Shinohara, H., Aiuppa, A., Giudice, G., Gurrieri, S. & Liuzzo, M. Variation of H₂O/CO₂ and CO₂/SO₂ ratios of volcanic gases discharged by continuous degassing of Mount Etna volcano, Italy. *J. Geophys. Res.: Solid Earth* (1978–2012), **113**, <https://doi.org/10.1029/2007jb005185> (2008).
53. Goepfert, K. & Gardner, J. E. Influence of pre-eruptive storage conditions and volatile contents on explosive Plinian style eruptions of basic magma. *Bullet. Volcanol.* **72**, 511–521 (2010).
54. Papale, P. & Polacci, M. Role of carbon dioxide in the dynamics of magma ascent in explosive eruptions. *Bullet. Volcanol.* **60**, 583–594 (1999).
55. Bamber, E. C. et al. Pre-and syn-eruptive conditions of a basaltic Plinian eruption at Masaya Volcano, Nicaragua: The Masaya Triple Layer (2.1 ka). *J. Volcanol. Geother. Res.* **392**, 106761 (2020).
56. Rowe, M. C. et al. Tarawera 1886: an integrated review of volcanological and geochemical characteristics of a complex basaltic eruption. *N. Zealand J. Geol. Geophys.* 1–24, <https://doi.org/10.1080/00288306.2021.1914118> (2021).
57. Adams, B. M. et al. DAKOTA, A Multilevel Parallel Object-Oriented Framework for Design Optimization, Parameter Estimation, Uncertainty Quantification, and Sensitivity Analysis Version 6.6 User's Manual, <https://doi.org/10.2172/1817318> (2017).
58. Alfano, F. et al. Subplinian monogenetic basaltic eruption of Sunset Crater, Arizona, USA. *GSA Bulletin*. **131**, 661–674 (2019).
59. Deegan, F. M. et al. Magma–carbonate interaction processes and associated CO₂ release at Merapi Volcano, Indonesia: insights from experimental petrology. *J. Petrol.* **51**, 1027–1051 (2010).
60. Freda, C. et al. Magma–carbonate interaction: an experimental study on ultrapotassic rocks from Alban Hills (Central Italy). *Lithos* **101**, 397–415 (2008).
61. Tait, S. R., Jaupart, C. & Vergnolle, S. Pressure, gas content and eruption periodicity of a shallow, crystallising magma chamber. *Earth Planetary Sci. Lett.* **92**, 107–123 (1989).
62. Corsaro, R. A., Di Renzo, V., Distefano, S., Miraglia, L. & Civetta, L. Relationship between petrologic processes in the plumbing system of Mt. Etna and the dynamics of the eastern flank from 1995 to 2005. *J. Volcanol. Geother. Res.* **251**, 75–89 (2013).
63. Brown, G. O. The history of the Darcy-Weisbach equation for pipe flow resistance. In: *Environmental and Water Resources History*, 34–43, [https://doi.org/10.1061/40650\(2003\)4](https://doi.org/10.1061/40650(2003)4) (2003).
64. Zein, A., Hantke, M. & Warnecke, G. Modeling phase transition for compressible two-phase flows applied to metastable liquids. *J. Comput. Phys.* **229**, 2964–2998 (2010).
65. Costa, A. Viscosity of high crystal content melts: Dependence on solid fraction. *Geophys. Res. Lett.* **32**, L22308 (2005).
66. Giordano, D., Russell, J. K. & Dingwell, D. B. Viscosity of magmatic liquids: a model. *Earth Planetary Sci. Lett.* **271**, 123–134 (2008).
67. Costa, A., Caricchi, L. & Bagdassarov, N. A model for the rheology of particle-bearing suspensions and partially molten rocks. *Geochem. Geophys. Geosyst.* **10**, Q0301 (2009).
68. Vona, A., Romano, C., Dingwell, D. B. & Giordano, D. The rheology of crystal-bearing basaltic magmas from Stromboli and Etna. *Geochim. et Cosmochim. Acta* **75**, 3214–3236 (2011).
69. Smith, P. M. & Asimow, P. D. Adiaab1ph: a new public front-end to the MELTS, pMELTS, and pHMELTS models. *Geochem. Geophys. Geosyst.* **6**, <https://doi.org/10.1029/2004gc000816> (2005).
70. Ghorso, M. S. & Sack, R. O. Chemical mass transfer in magmatic processes IV. A revised and internally consistent thermodynamic model for the interpolation and extrapolation of liquid-solid equilibria in magmatic systems at elevated temperatures and pressures. *Contrib. Mineral. Petrol.* **119**, 197–212 (1995).
71. Fang, X., Xu, Y. & Zhou, Z. New correlations of single-phase friction factor for turbulent pipe flow and evaluation of existing single-phase friction factor correlations. *Nuclear Eng. Design* **241**, 897–902 (2011).
72. Degruyter, W., Bachmann, O., Burgisser, A. & Manga, M. The effects of outgassing on the transition between effusive and explosive silicic eruptions. *Earth Planetary Sci. Lett.* **349**, 161–170 (2012).
73. Woods, A. W. & Koyaguchi, T. Transitions between explosive and effusive eruptions of silicic magmas. *Nature* **370**, 641–644 (1994).
74. Gonnermann, H. M. & Manga, M. The fluid mechanics inside a volcano. *Ann. Rev. Fluid Mech.* **39**, 321–356 (2007).
75. Sparks, R. S. J. Dynamics of magma degassing. *Geol. Soc. London Special Publ.* **213**, 5–22 (2003).
76. Rust, A. C. & Cashman, K. V. Permeability of vesicular silicic magma: inertial and hysteretic effects. *Earth Planetary Sci. Lett.* **228**, 93–107 (2004).
77. Pioli, L. et al. Experimental constraints on the outgassing dynamics of basaltic magmas. *J. Geophys. Res.: Solid Earth* **117**, B03204 (2012).

78. Yoshida, S. & Koyaguchi, T. A new regime of volcanic eruption due to the relative motion between liquid and gas. *J. Volcanol. Geother. Res.* **89**, 303–315 (1999).
79. Papale, P. Strain-induced magma fragmentation in explosive eruptions. *Nature* **397**, 425–428 (1999).
80. Holloway, J. R. & Blank, J. G. Application of experimental results to COH species in natural melts. *Rev. Mineral.* **30**, 187–187 (1994).
81. La Spina, G., de'Michieli Vitturi, M. & Romenski, E. A compressible single-temperature conservative two-phase model with phase transitions. *Int. J. Numerical Methods Fluids* **76**, 282–311 (2014).
82. La Spina, G., de'Michieli Vitturi, M. & Clarke, A. B. Transient numerical model of magma ascent dynamics: application to the explosive eruptions at the Soufrière Hills Volcano. *J. Volcanol. Geother. Res.* **336**, 118–139 (2017b).
83. de'Michieli Vitturi, M., Clarke, A. B., Neri, A. & Voight, B. Effects of conduit geometry on magma ascent dynamics in dome-forming eruptions. *Earth Planetary Sci. Lett.* **272**, 567–578 (2008).
84. La Spina, G. & de'Michieli Vitturi, M. MAMMA_CODE_v2022_03_31.zip. *Figshare. Software.*, <https://doi.org/10.6084/m9.figshare.19361981.v1> (2022).

Acknowledgements

Sensitivity analyses were performed on the ARCHER2 National Supercomputing Service. The research leading to these results has received funding from the RCUK NERC Dis-Eqm project (NE/N018575/1). A.B.C.'s participation was funded through the US NSF (EAR-1642569). Finally, we gratefully acknowledge three anonymous reviewers for their useful and constructive comments, which improved this paper.

Author contributions

G.L.S., F.A., M.R.B., M.P., A.B.C. contributed equally on the conceptualisation of the work, on the interpretation of the results, and on the writing of the paper. G.L.S. performed the numerical simulations and plotted the results.

Competing interests

The authors declare no competing interests.

Additional information

Supplementary information The online version contains supplementary material available at <https://doi.org/10.1038/s43247-022-00479-6>.

Correspondence and requests for materials should be addressed to Giuseppe La Spina.

Peer review information *Communications Earth & Environment* thanks the anonymous reviewers for their contribution to the peer review of this work. Primary Handling Editors: Maria Luce Frezzotti, Joe Aslin.

Reprints and permission information is available at <http://www.nature.com/reprints>

Publisher's note Springer Nature remains neutral with regard to jurisdictional claims in published maps and institutional affiliations.



Open Access This article is licensed under a Creative Commons Attribution 4.0 International License, which permits use, sharing, adaptation, distribution and reproduction in any medium or format, as long as you give appropriate credit to the original author(s) and the source, provide a link to the Creative Commons license, and indicate if changes were made. The images or other third party material in this article are included in the article's Creative Commons license, unless indicated otherwise in a credit line to the material. If material is not included in the article's Creative Commons license and your intended use is not permitted by statutory regulation or exceeds the permitted use, you will need to obtain permission directly from the copyright holder. To view a copy of this license, visit <http://creativecommons.org/licenses/by/4.0/>.

© The Author(s) 2022